Supplementary materials:

Rainwater isotopic composition in the Ecuadorian Andes and Amazon reflects cross-equatorial flow seasonality

Danny Vargas [1,*], Oscar Chimborazo [2], Elemér László [1], Marjan Temovski [1], and László Palcsu [1]

[1] Isotope Climatology and Environmental Research Centre, Institute for Nuclear Research, Debrecen H-4026, Hungary; danny.vargas@atomki.hu

[2] Yachay Tech University, School of Physical Sciences and Nanotechnology, 100119 Urcuquí, Ecuador; ochimborazo@yachaytech.edu.ec

(a)

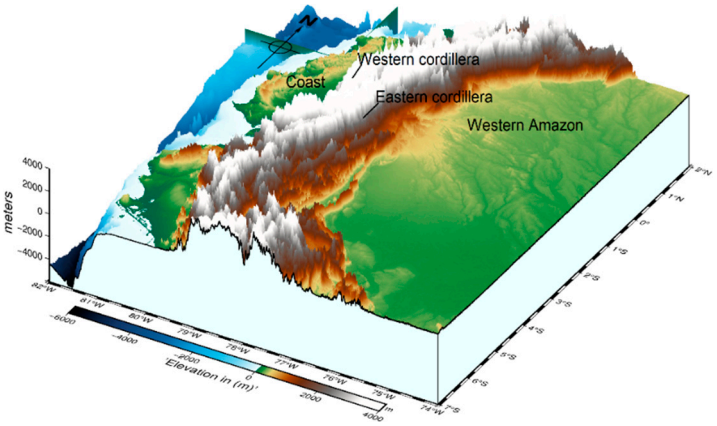

(b)

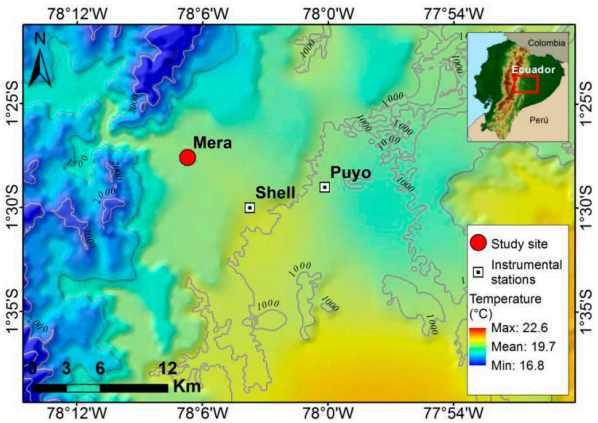

(c)

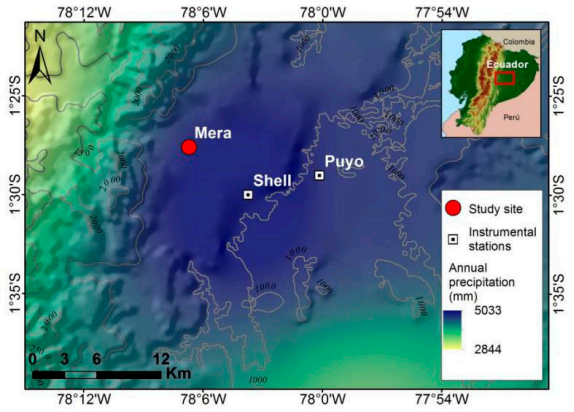

Figure S1. (**a**) Three-dimensional perspective of the topography of Ecuador. The western and eastern Andean cordillera clearly stands out and modulates the country's rainfall and temperature variations. The map was generated using the Python wrapper PyGMT for the Generic Mapping Tools (GMT) [85] (**b**) Map of isotherms and (**c**) isohyets of the Mera study site (red dot) with the two nearest instrumental stations Puyo and Shell.

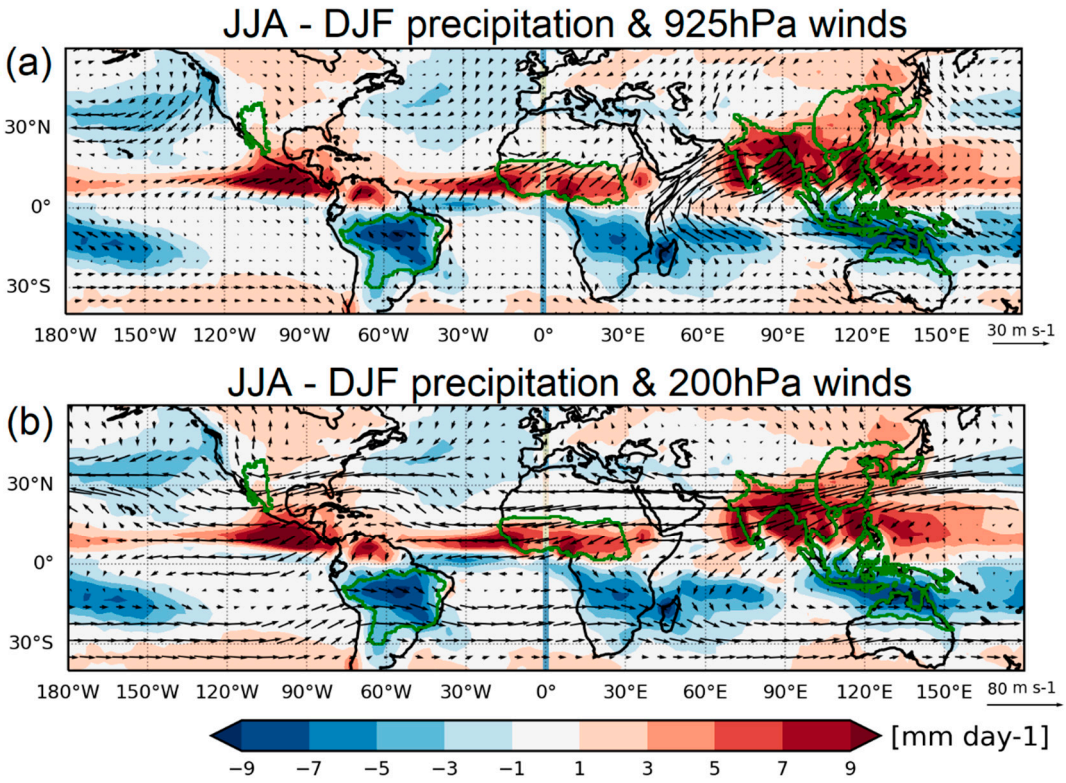

Figure S2. Climatological mean JJA (boreal summer) minus DJF (boreal winter) precipitation with **(a)** 925 hPa and **(b)** 200 hPa annual wind reversal (black arrows with corresponding speed scale at the bottom right). Red and blue areas show regions where the local summer minus winter precipitation exceeds 2 mm day$^{-1,}$ and summer accounts for at least 55% percent of the annual total rainfall [86]. Green lines indicate the six land monsoon regions defined in IPCC WGI Chapter 8 [87]. The borders of continental Ecuador are marked in both insets in South America. The enhanced monthly averaged precipitation values (mm day^{-1}) were obtained from CPC Merged Analysis of Precipitation (CMAP) which merges five kinds of satellite estimates with rain gauge data and blended NCEP-NCAR reanalysis [88]. The uv wind components at 925 and 200 hPa pressure levels from 1979 to 2010 correspond to ERA5 reanalysis [89].

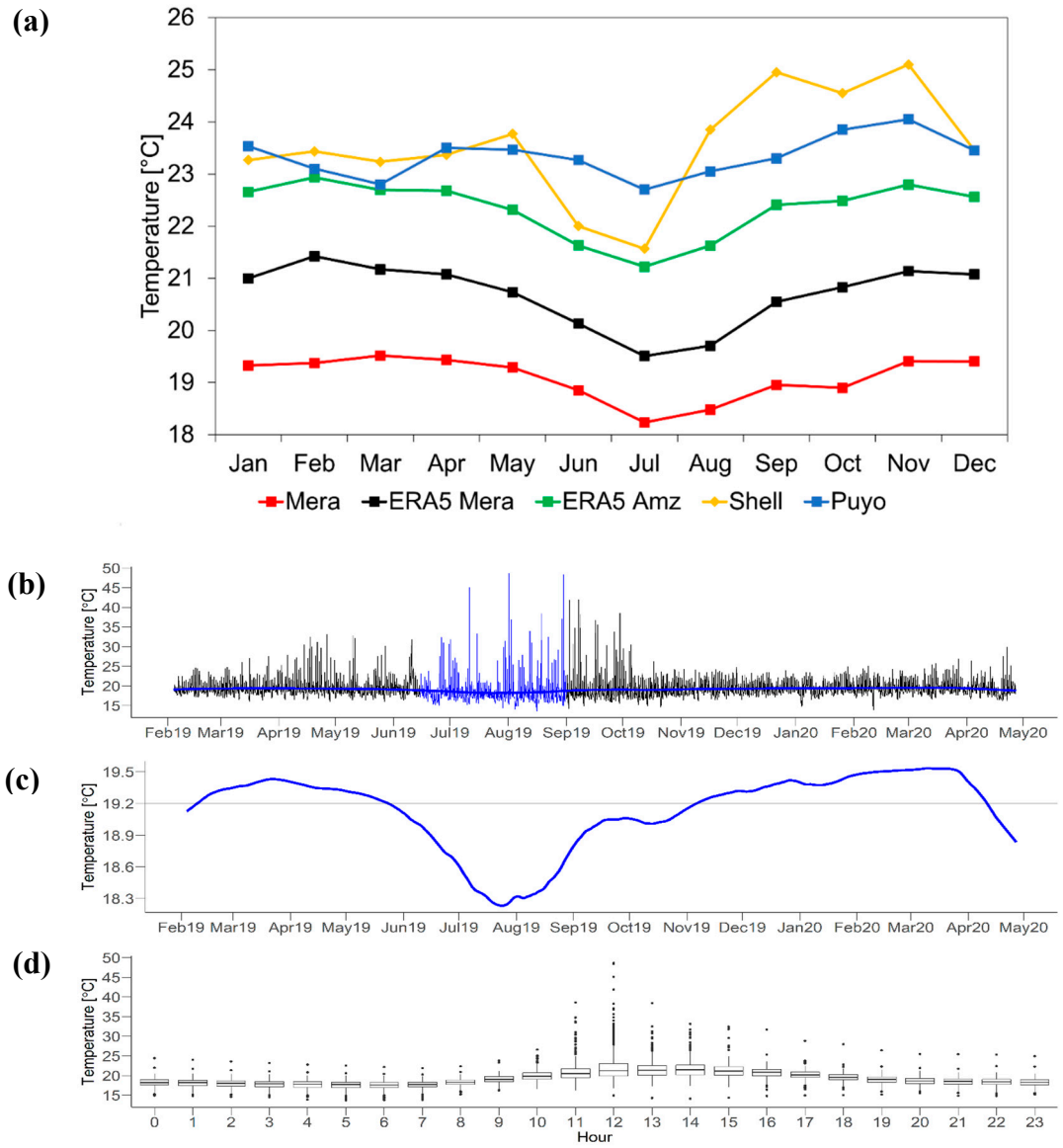

Figure S3. Seasonal temperature fluctuations in the Mera study site. (**a**) Comparison between the monitored monthly temperature (red line) with ERA5 reanalysis interpolated for Mera (black line) and the Ecuadorian Amazon (green line). The Shell and Puyo meteorological stations (yellow and blue lines) are also included. The common period 2019 to 2021 was used in all cases. (**b**) Temperature time-series from February 2019 to April 2020 monitoring campaign (14 months) in the Mera site at hourly resolution. Temperature drop and trend curve (Loess) were computed using Multiple Seasonal Decomposition and are highlighted in blue. (**c**) Enlarged Loess trend (blue horizontal line in plot (b) with average temperature (black line) calculated for the monitoring period. There is a minimum seasonal variation throughout the year except in July and August, where a 1°C decrease below the annual mean (black horizontal line) is observed. (**d**) Monitored temperature boxplot showing daily fluctuations. The time interval from 10 am to 4 pm is the warmest during the day, with temperatures above 30 °C. Minimum temperatures are found in earlier mornings and late nights.

Lago Agrio

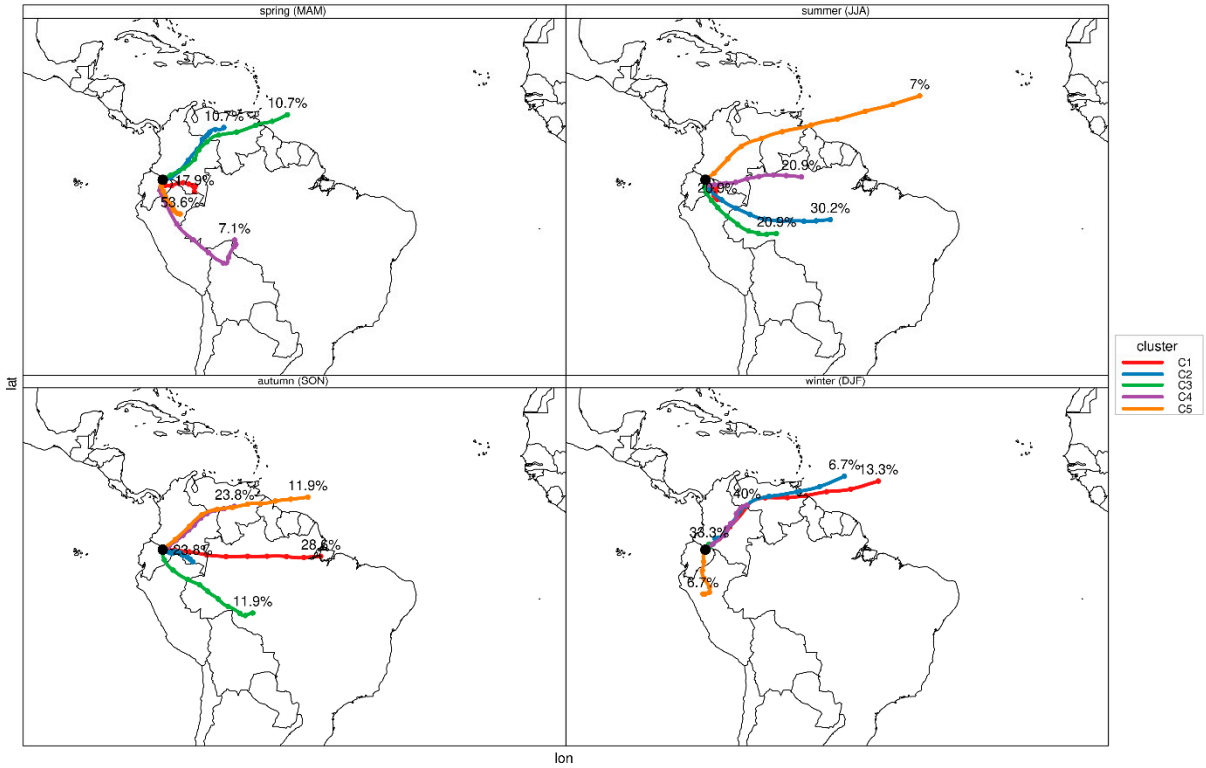

Nuevo Rocafuerte

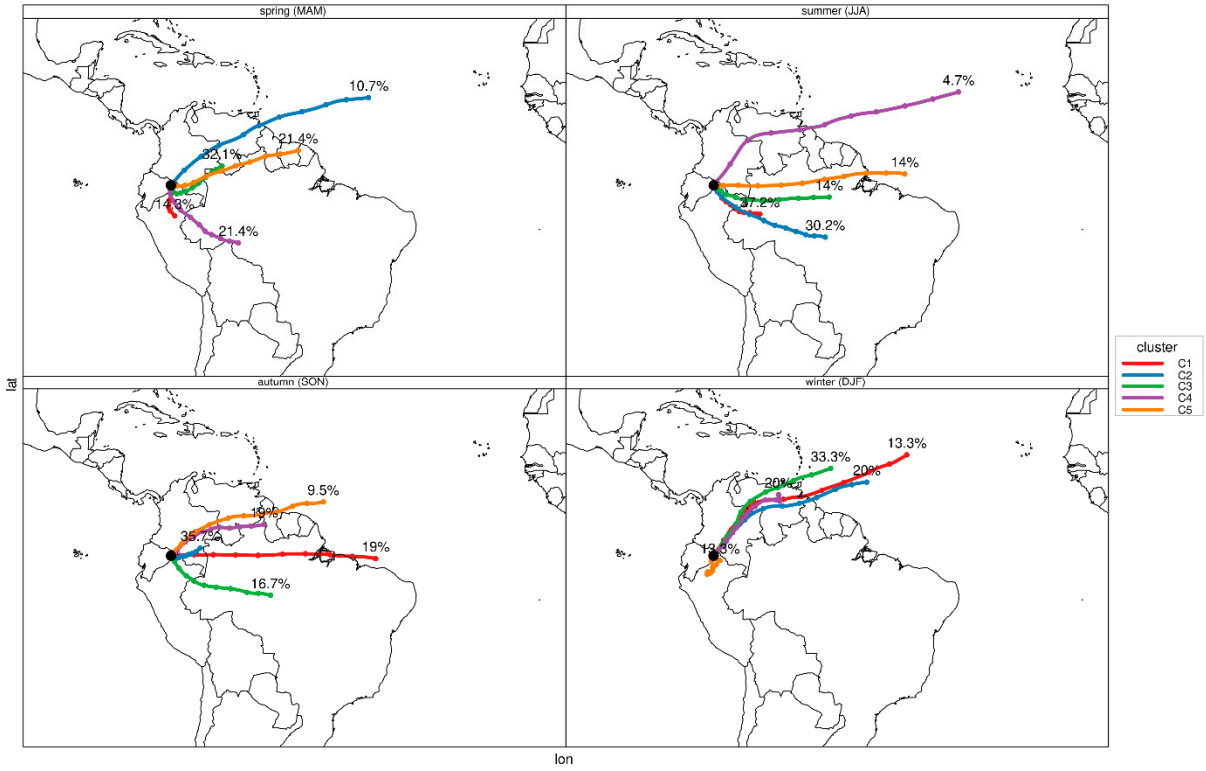

Izobamba

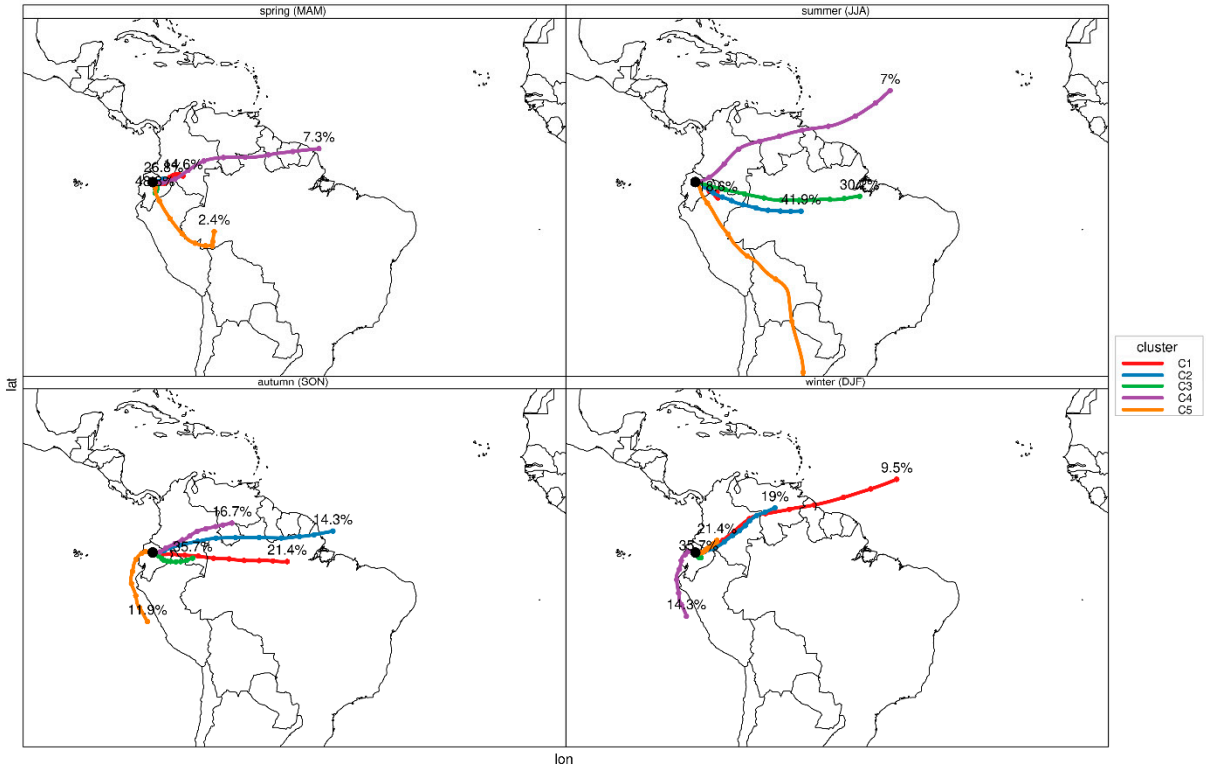

Quito

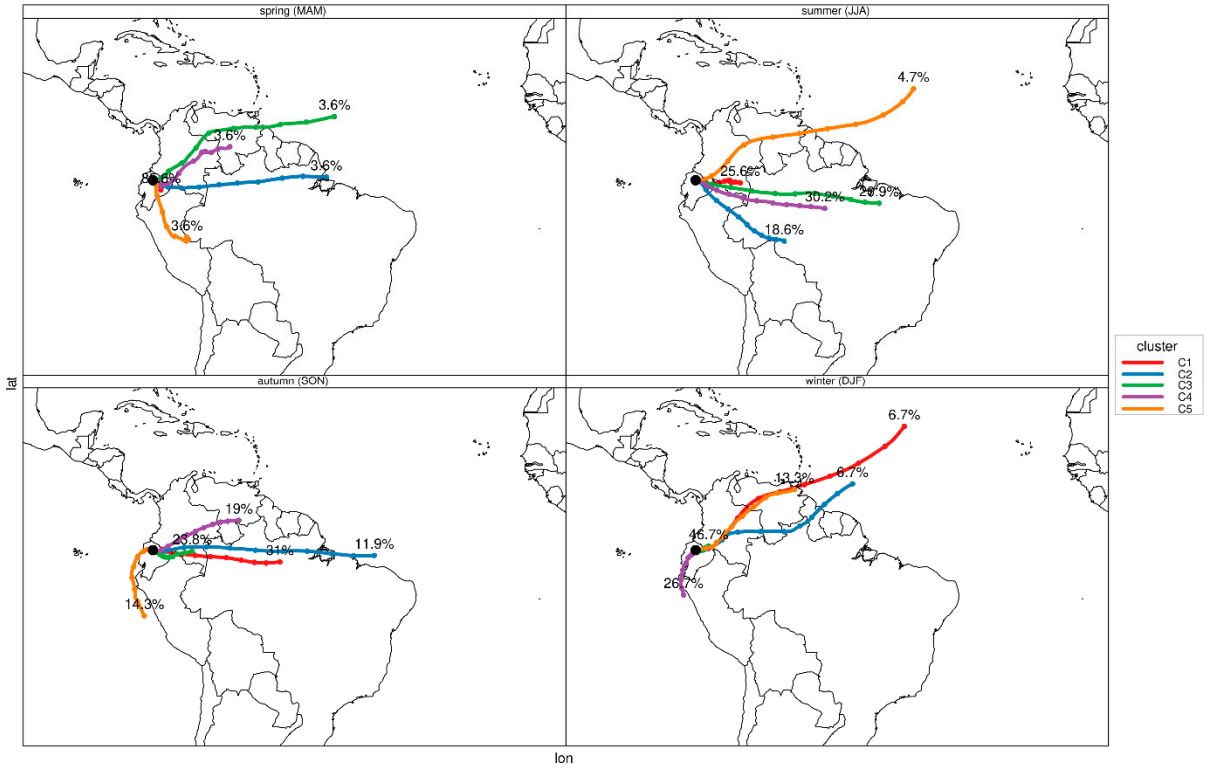

Papallacta

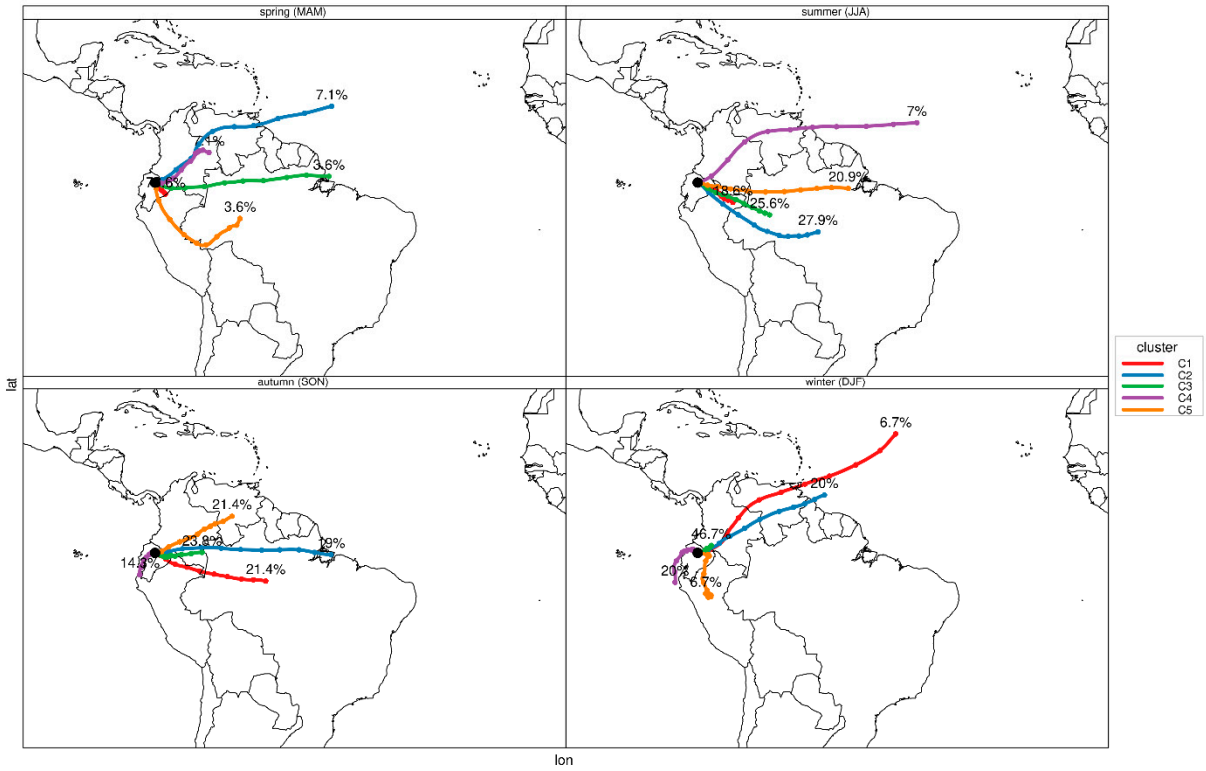

Mera

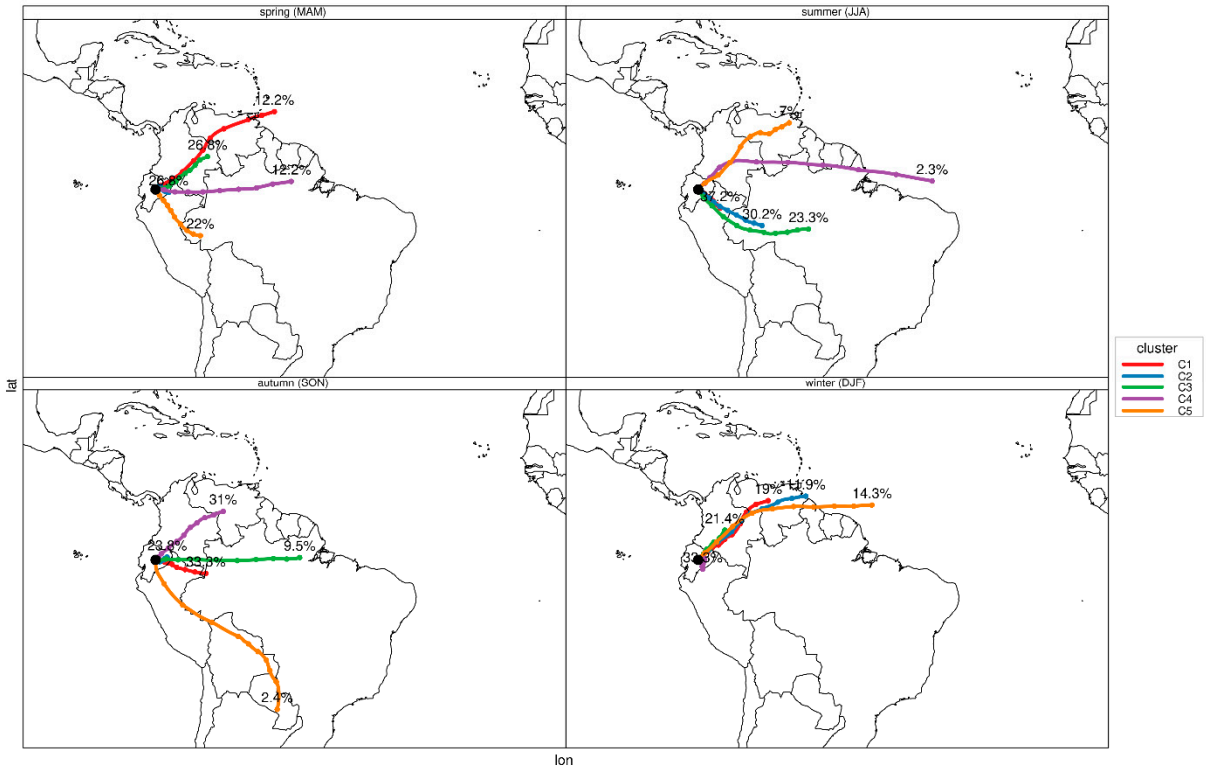

Amaluza

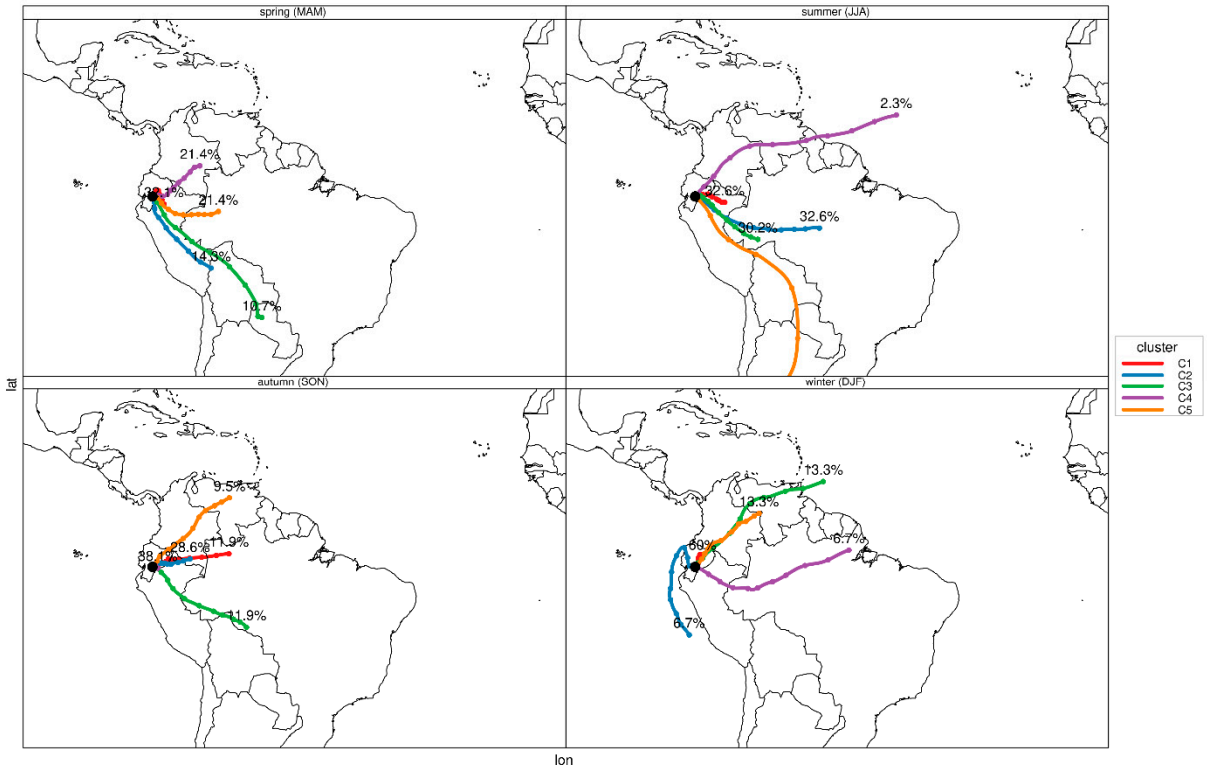

Mendez

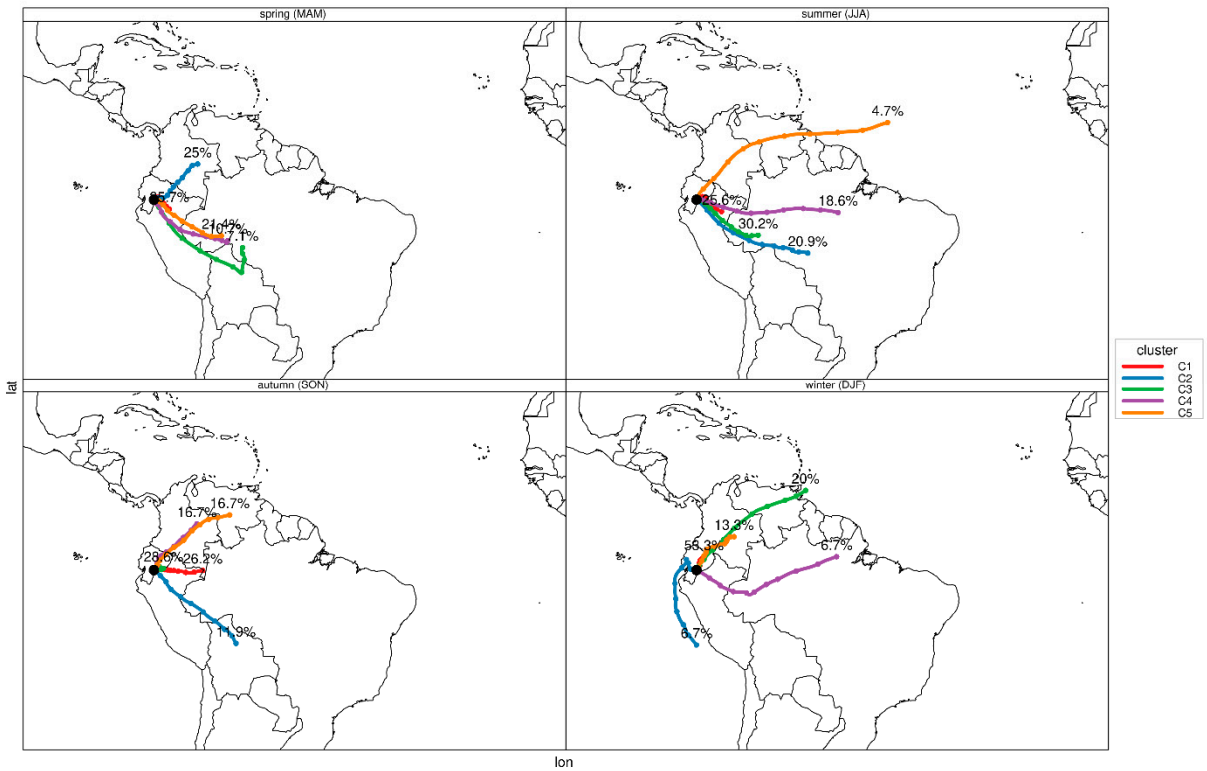

Cuenca

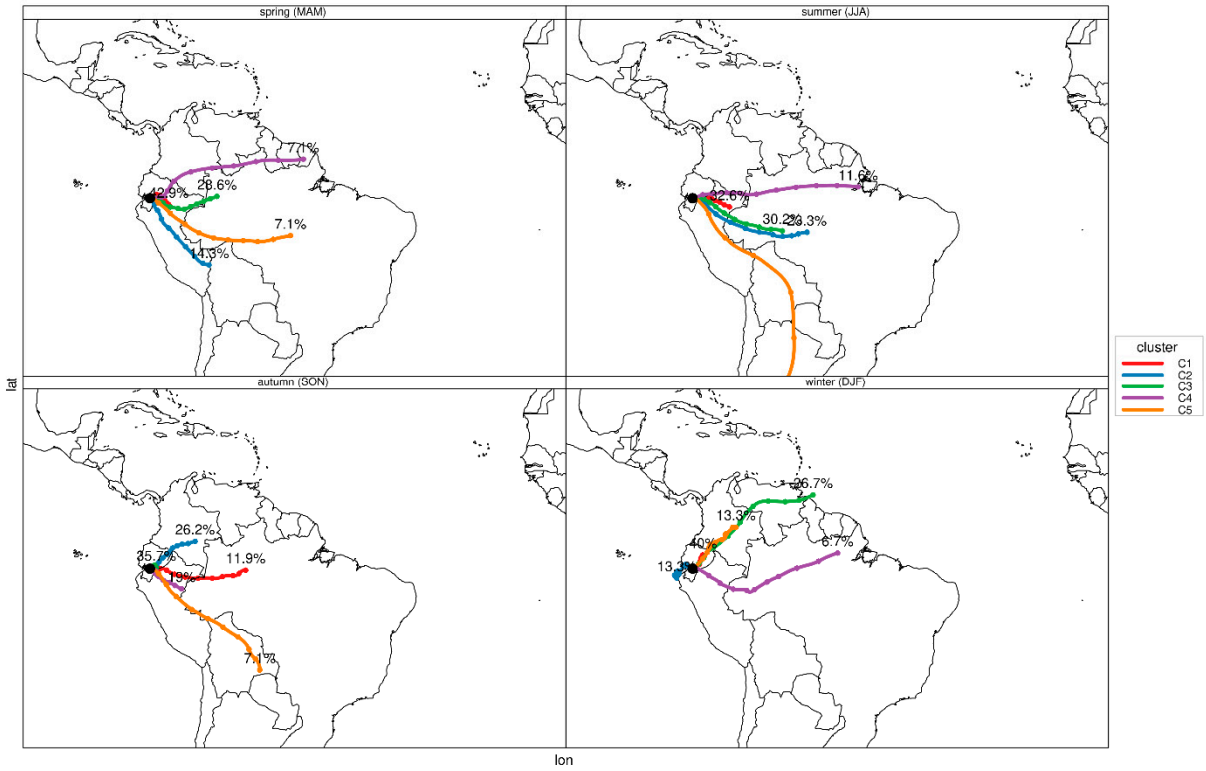

Zhurucay

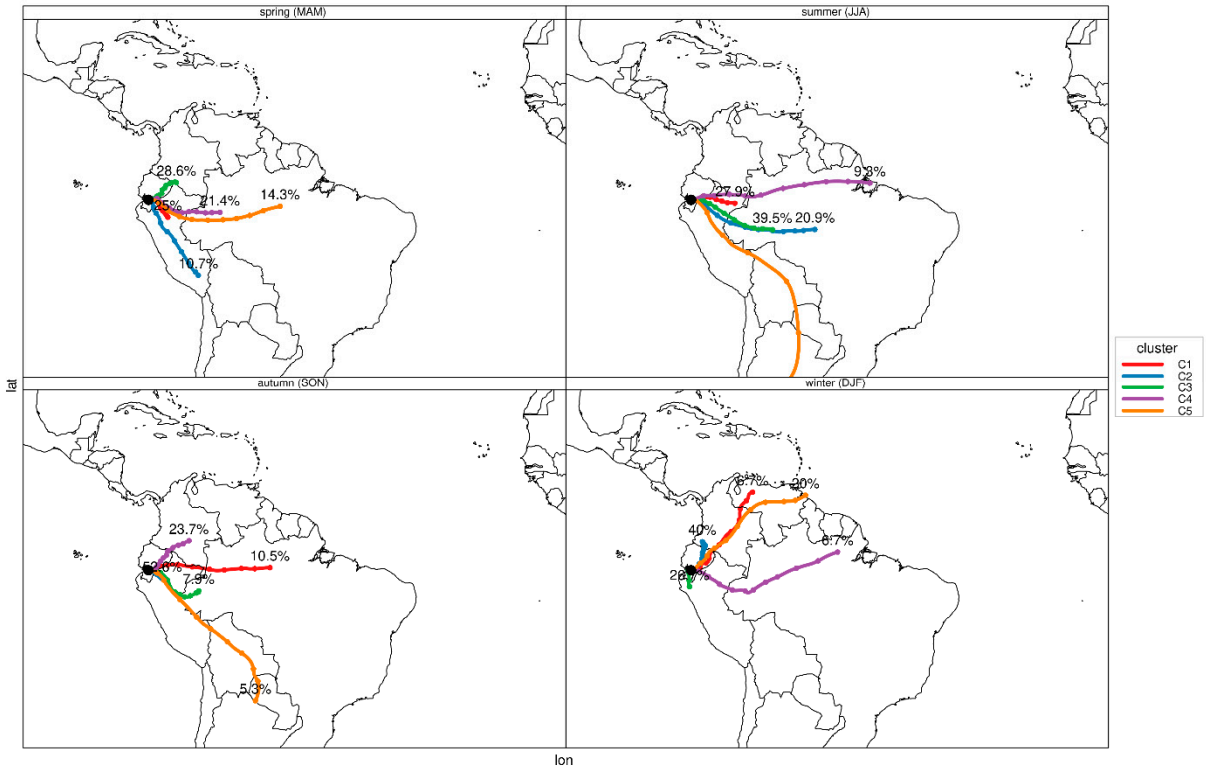

ECSF

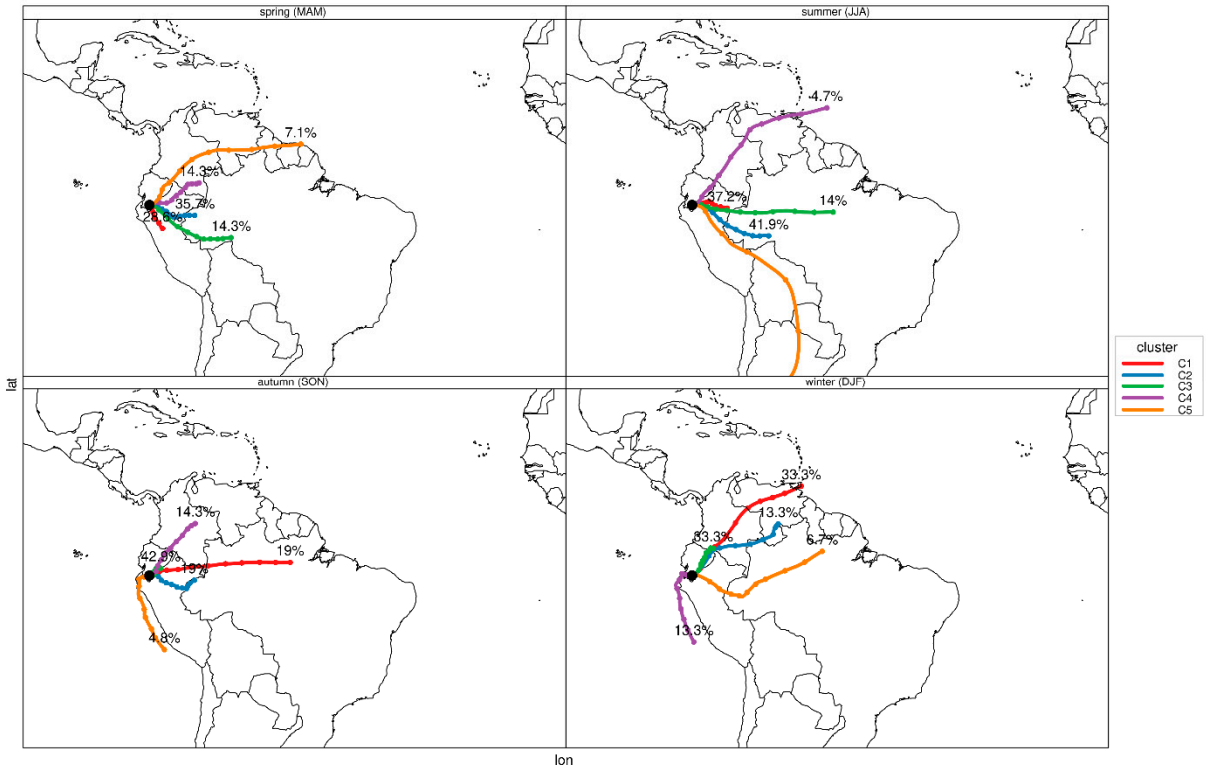

El Chaco

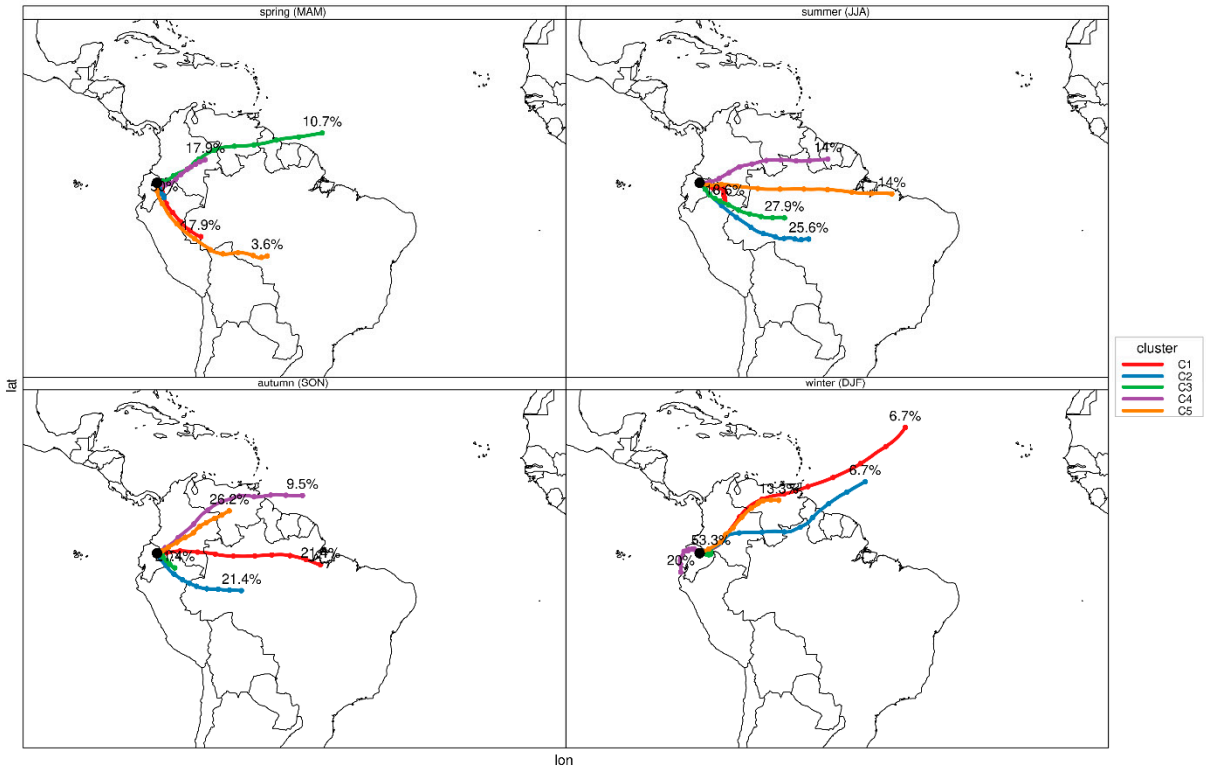

Cuyuja

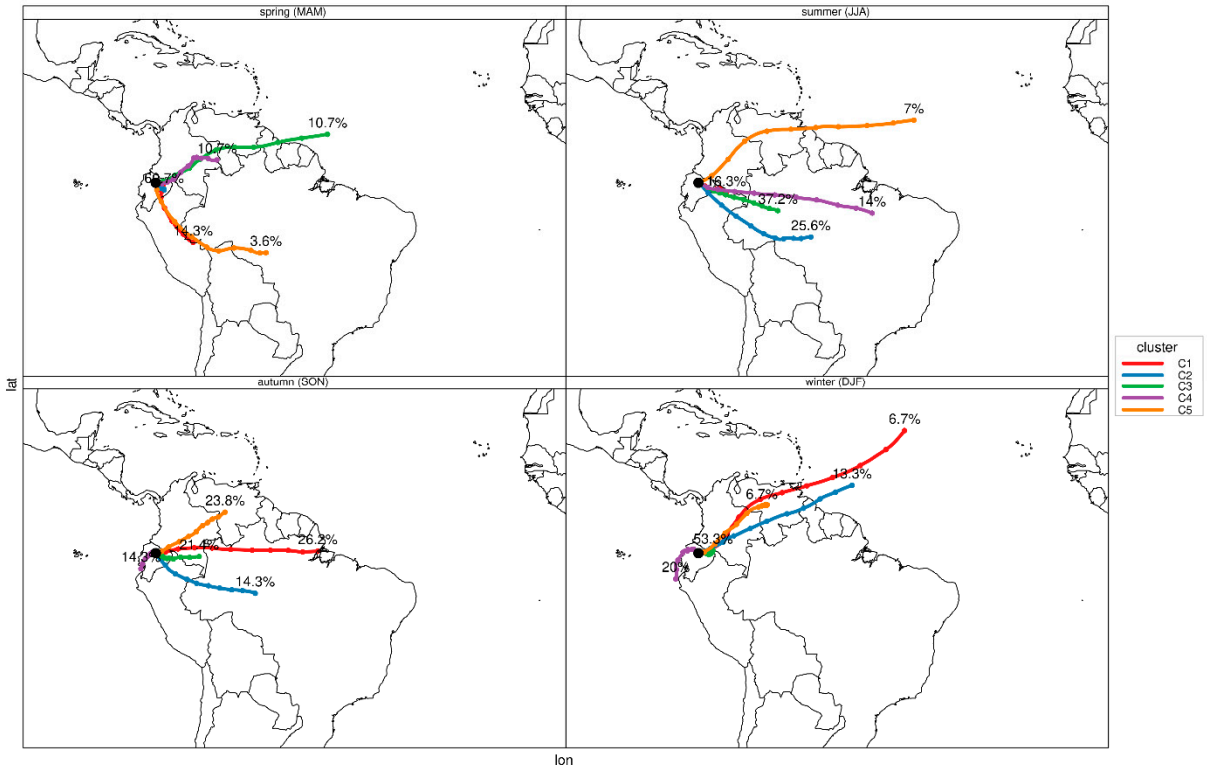

Cajas

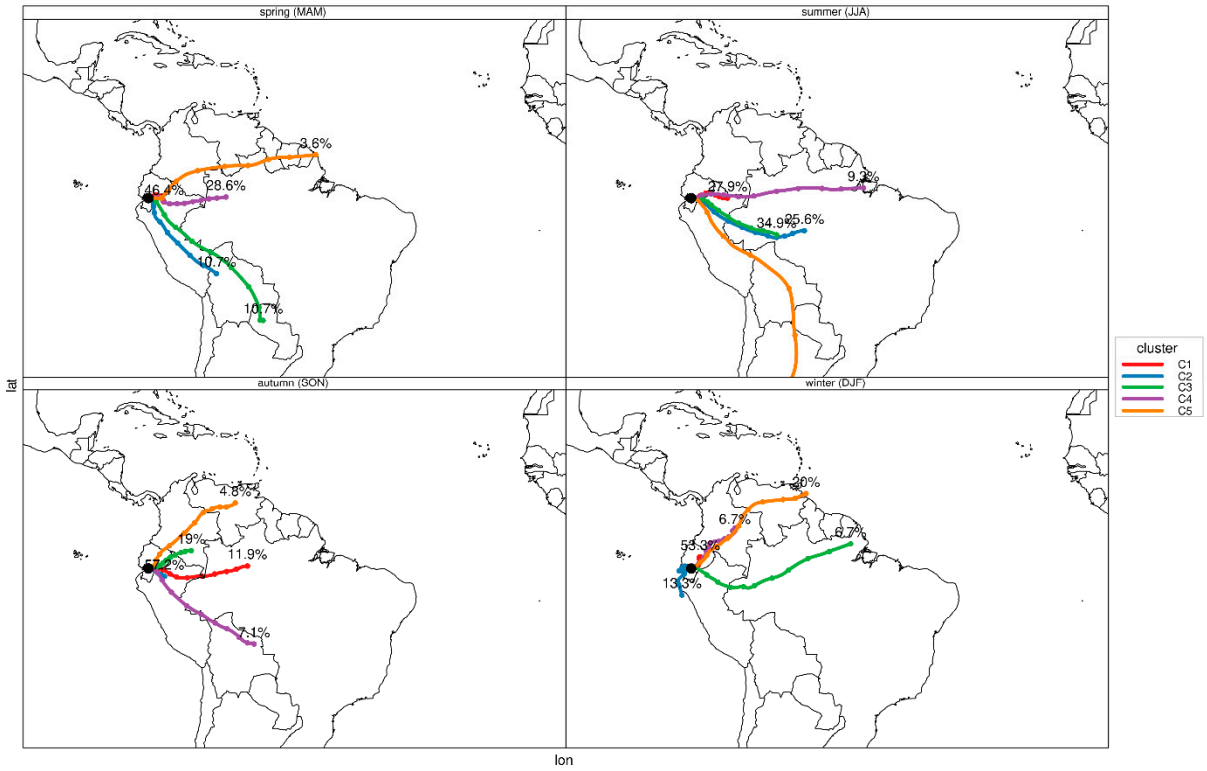

Alluriquin

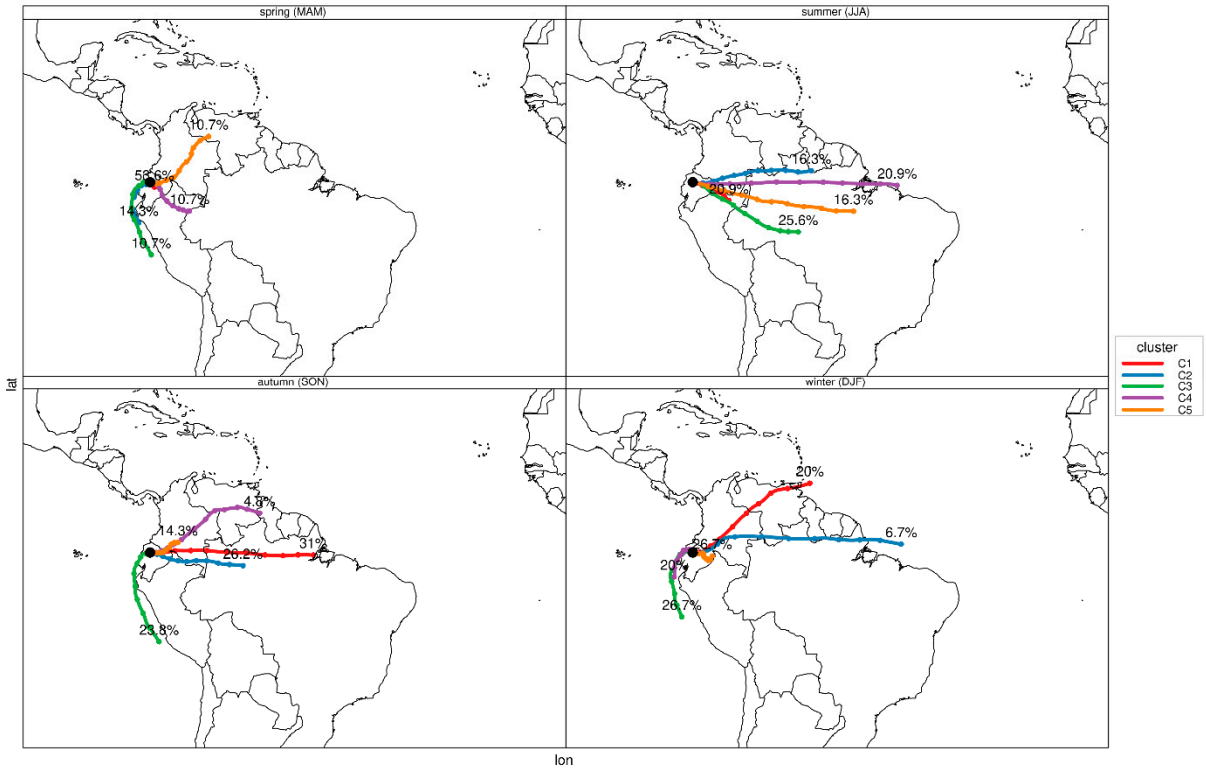

Baeza

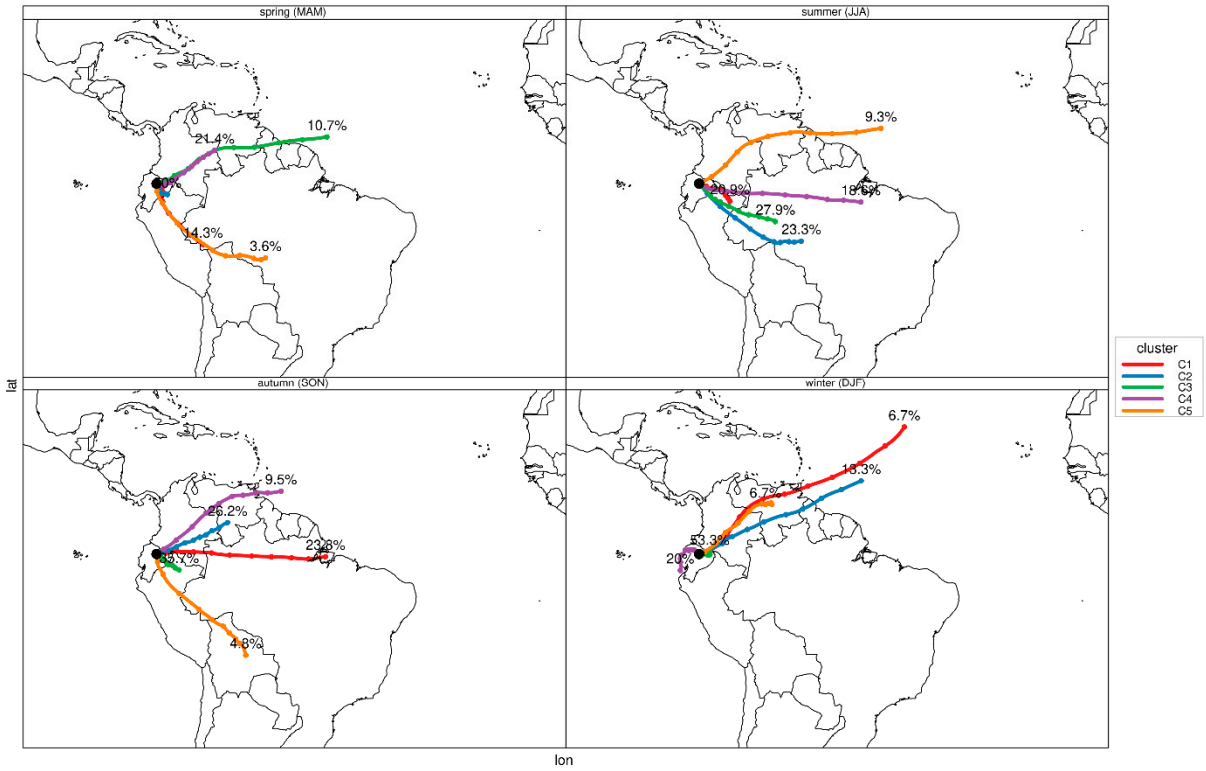

Figure S4. Cluster analysis on back trajectories using the Euclidean distance between two trajectories for the stations indicated in Figure 2. The mean trajectory for each cluster is plotted using a 5-cluster solution for the year 2019 for 120 h (5 days). Seasons are referred to the Northern hemisphere (boreal winter DJF, spring MAM, summer JJA and autumn SON).

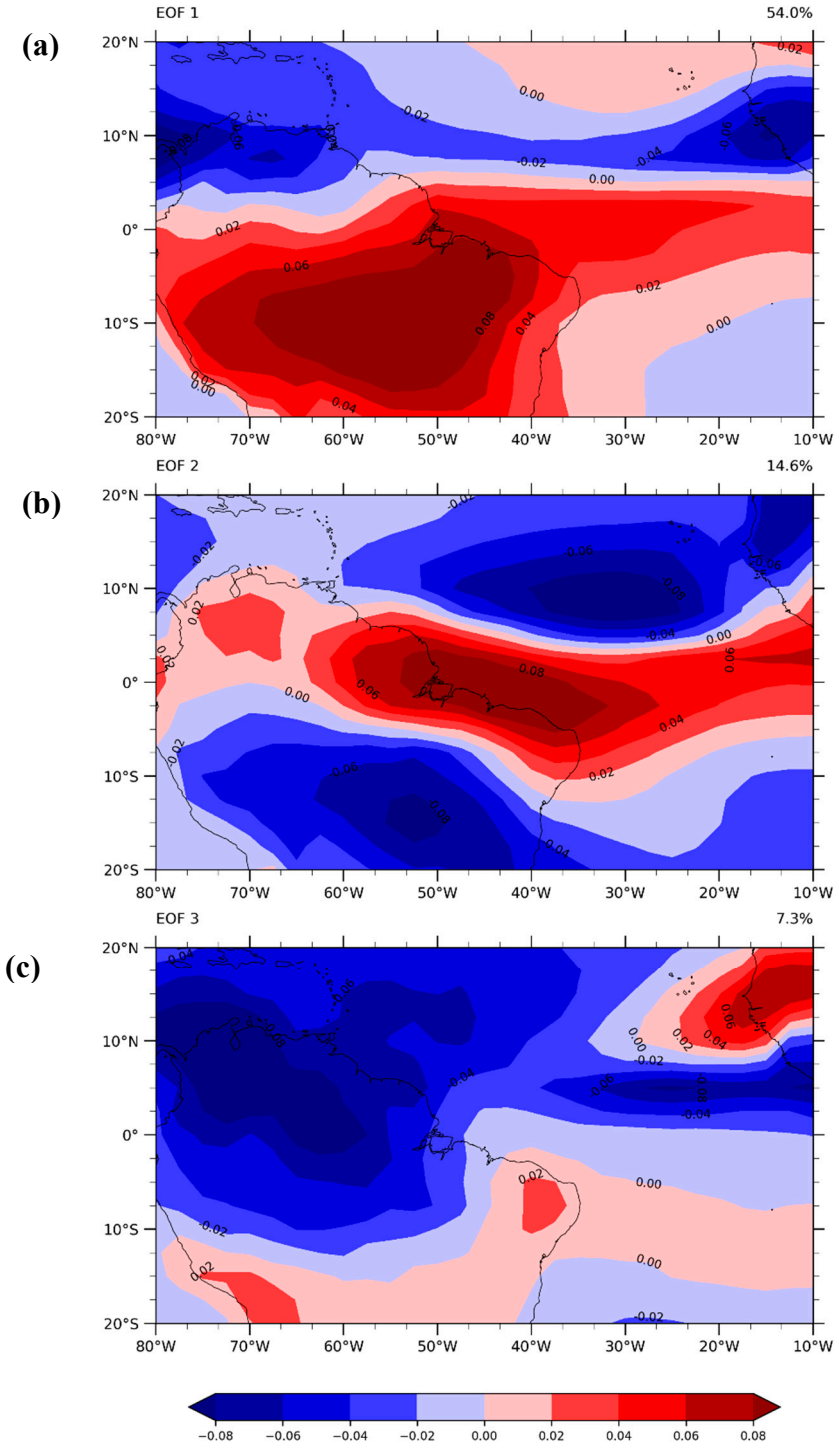

Figure S5. The first EOF mode patterns of the OLR in tropical South America as described by Garcia et al. [36] (**a**) EOF1 corresponds to the SAMS (**b**) EOF2 corresponds to the ITCZ and **(c)** EOF3 is associated to the equatorially symmetric mode which is the response of tropical convection to annual insolation on the equator. The calculation was performed using OLR monthly data from 1979 to 2020 from the National Oceanic and Atmospheric Administration (NOAA) polar-orbiting satellites interpolated at 2.5° x 2.5° [56].

DJF

500

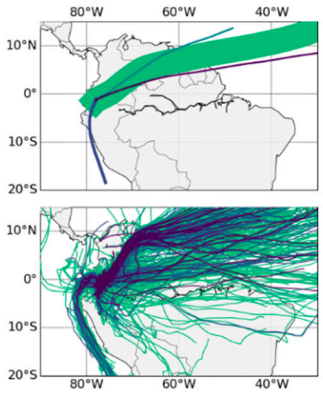

1000

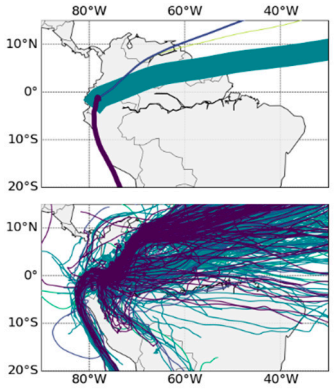

2000

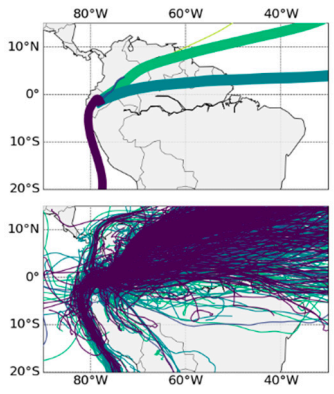

MAM

500

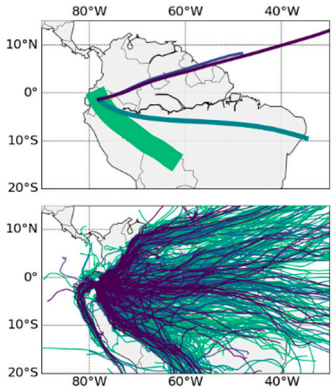

1000

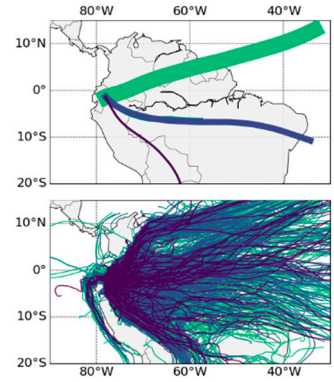

2000

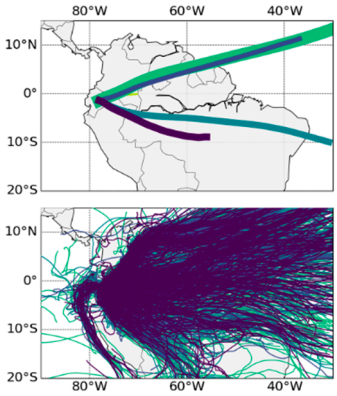

JJA

500

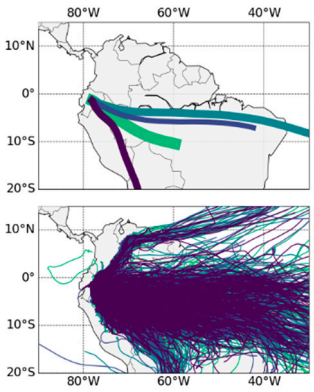

1000

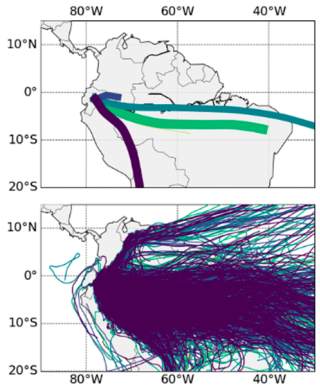

2000

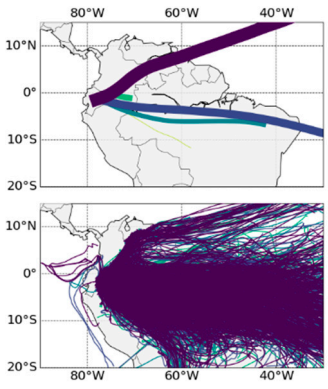

SON

500

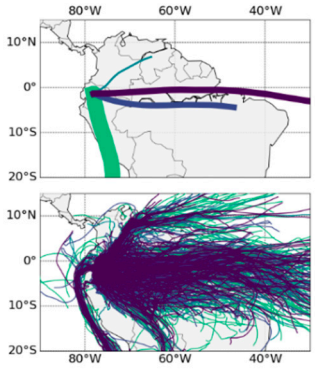

1000

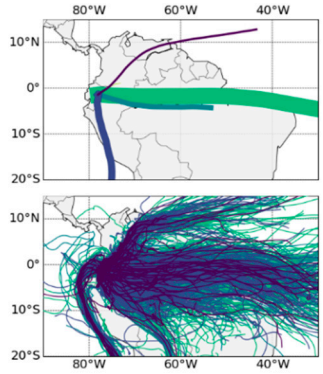

2000

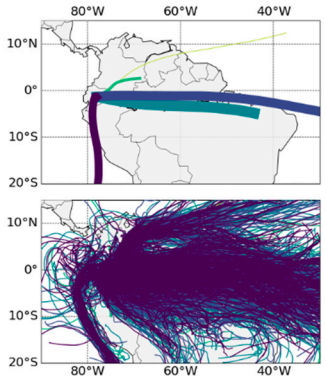

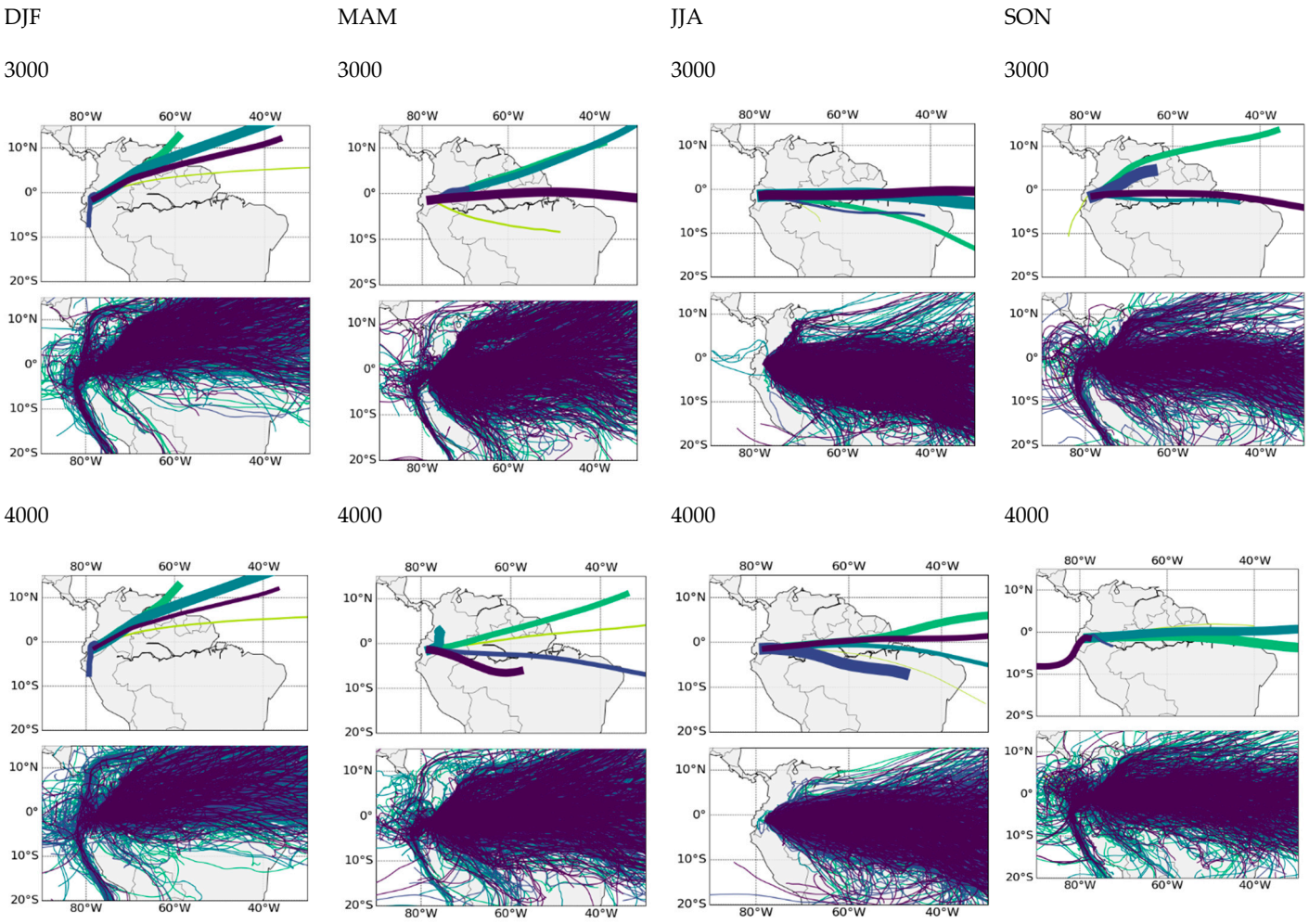

Figure S6. Back trajectories for the Mera site (2014-2019) for austral summer (DJF), autumn (MAM), winter (JJA) and spring (SON) at 500, 1000, 2000, 3000 and 4000 meters. **(Top)** Five main cluster paths indicating dominant trajectories. The line width represents the portion of trajectories that are members relative to the total number of trajectories clustered **(Bottom)** All trajectory paths. The trajectories were run using the PySplit Python package [49].

Jan

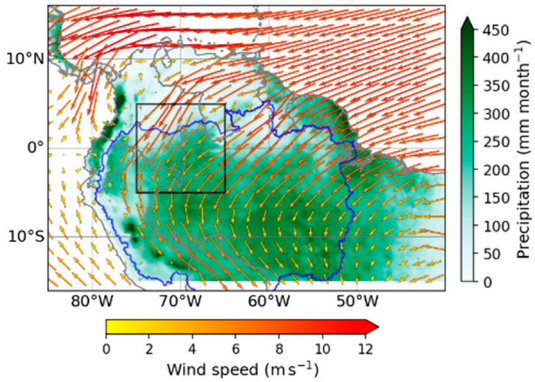

Feb

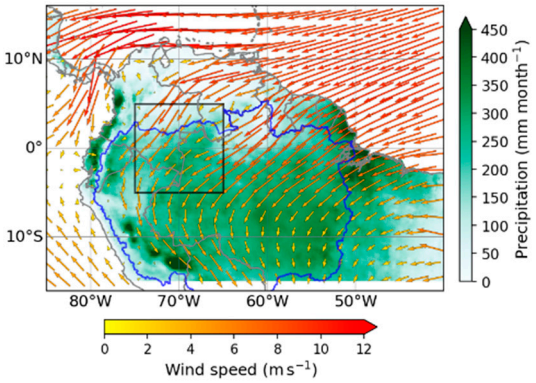

Mar

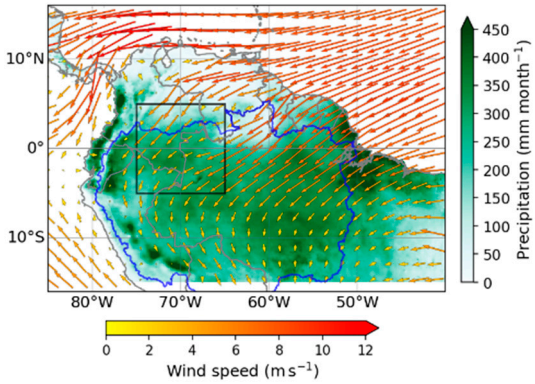

Apr

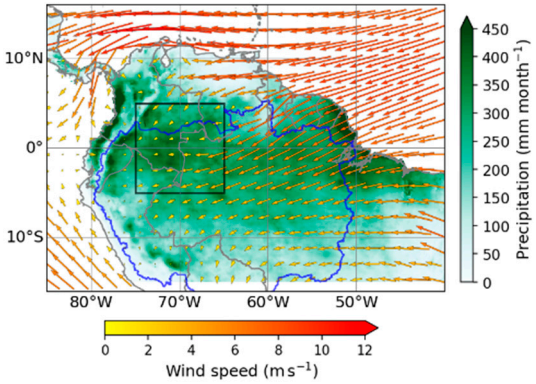

May

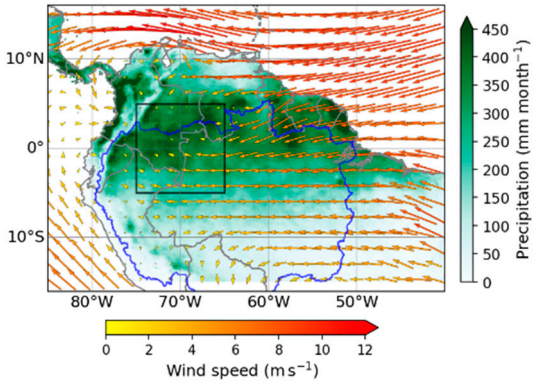

Jun

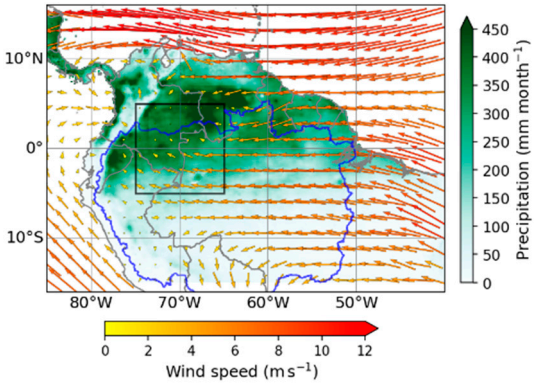

Jul

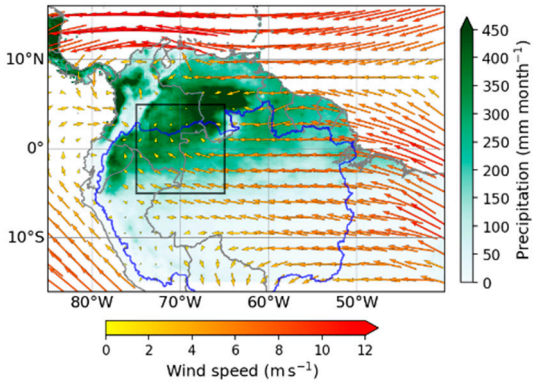

Aug

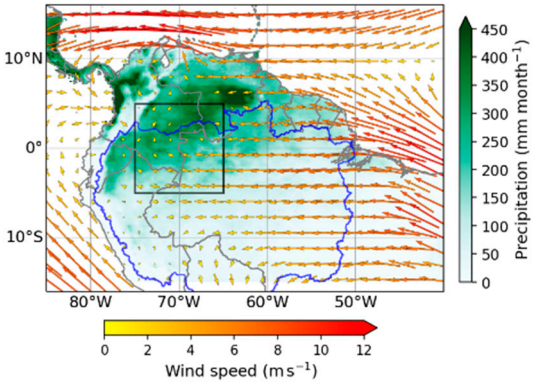

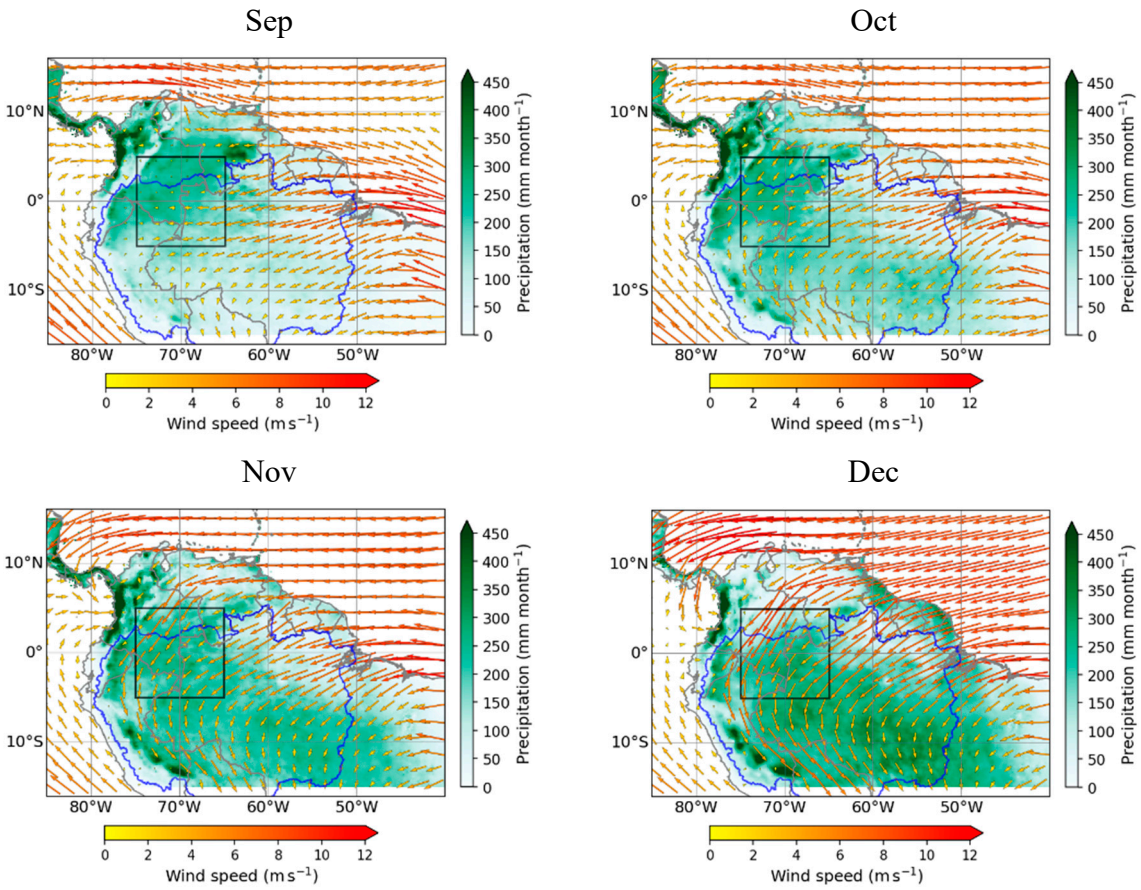

Figure. S7. Monthly wind vectors (arrows) at 950-850 hPa and long-term mean CHIRPS precipitation. The black box at 5°S-5°N, 65°-75°W over the western Amazon indicates the area where the seasonal reversal of the circulation is effectively observed according to Wang et al. [86] and represents the variability of the low-level cross-equatorial flow. The OLLJ is observable during austral summer (DJF) by the strong wind vectors crossing Venezuela, Colombia and reaching Ecuador. The boundaries of the Amazon basin are marked in blue.

Jan

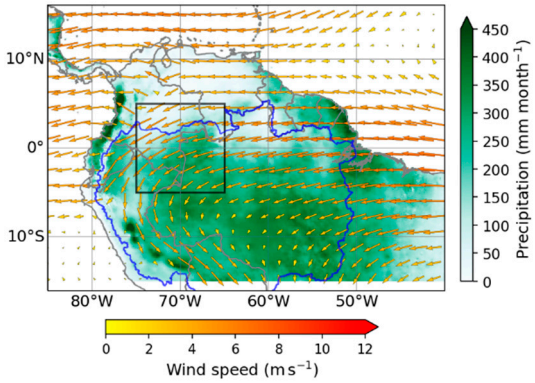

Feb

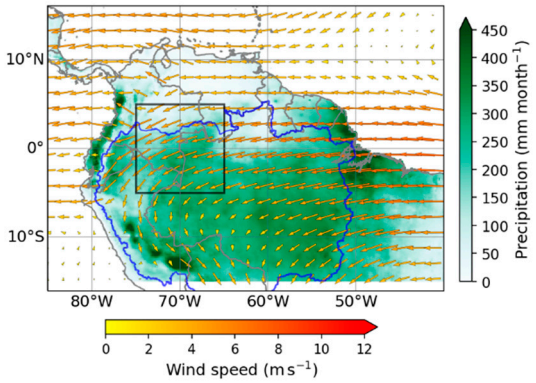

Mar

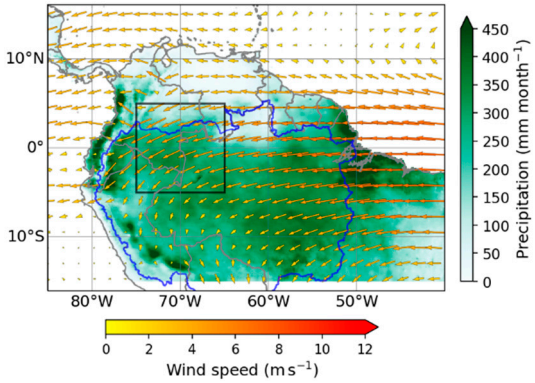

Apr

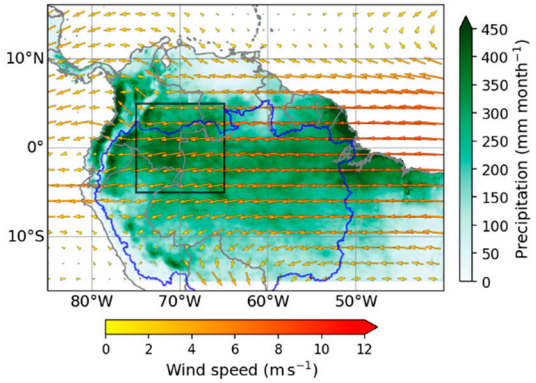

May

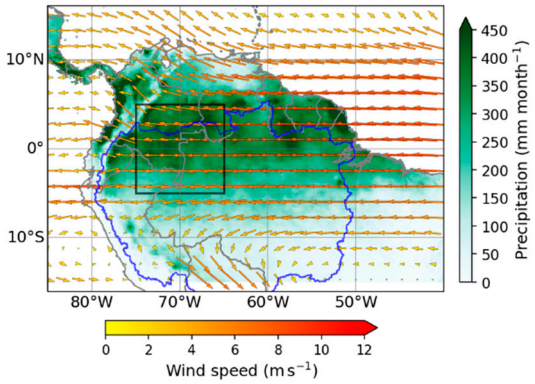

Jun

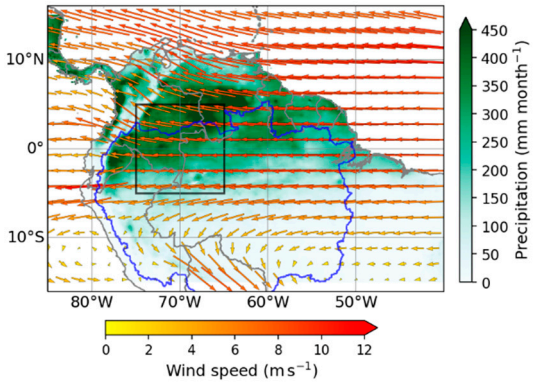

Jul

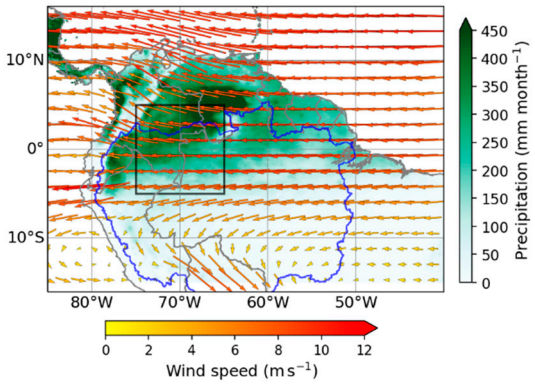

Aug

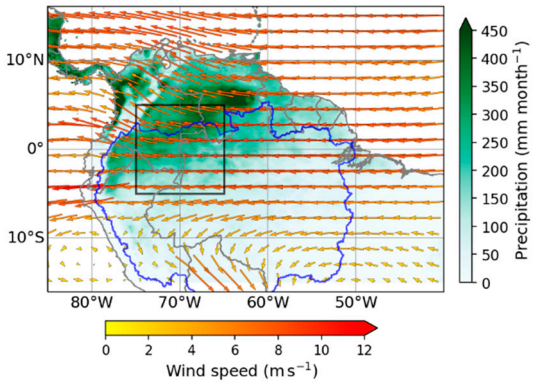

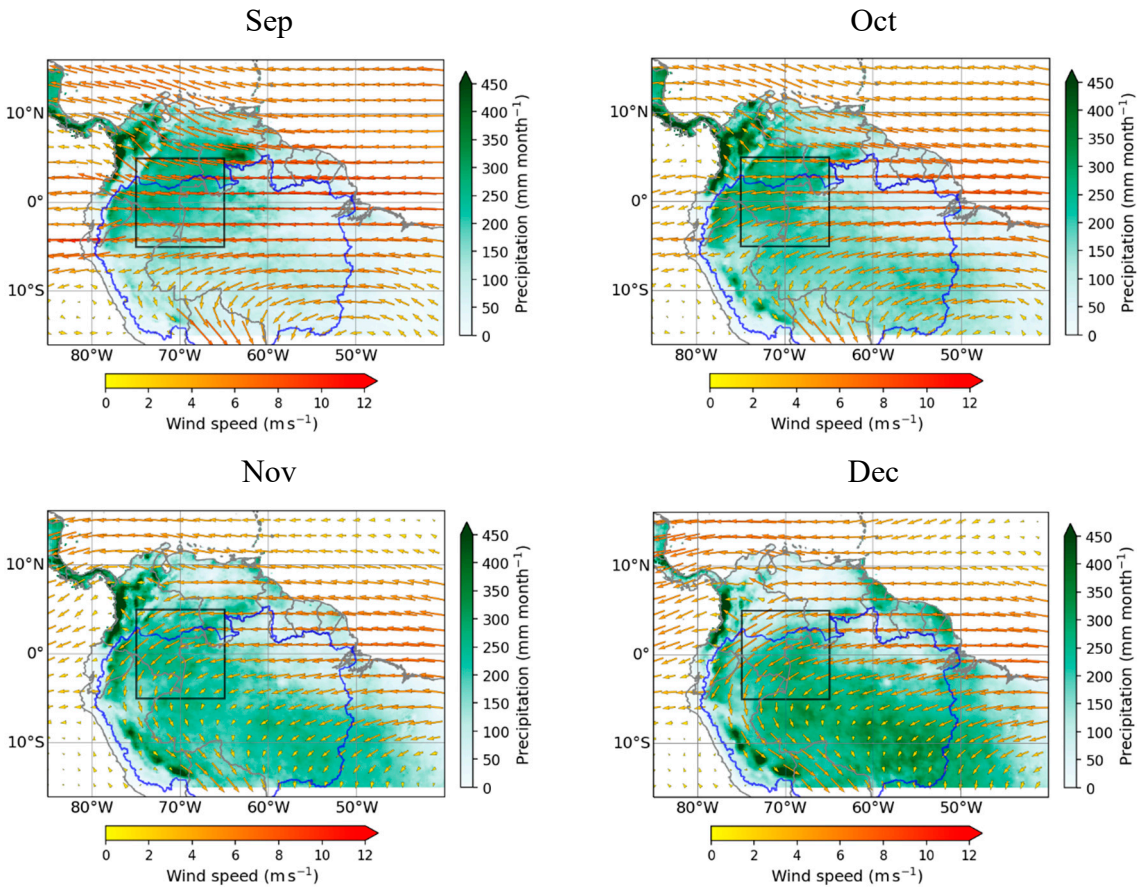

Figure S8. Same as Figure S7 but for 700-600 hPa. The equatorial mid-tropospheric easterly jet (EMTEJ) development is clearly observable from April to July moving from east to west and crossing the Amazon basin.

Lago Agrio

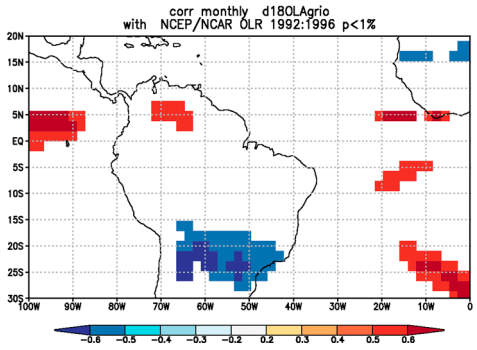

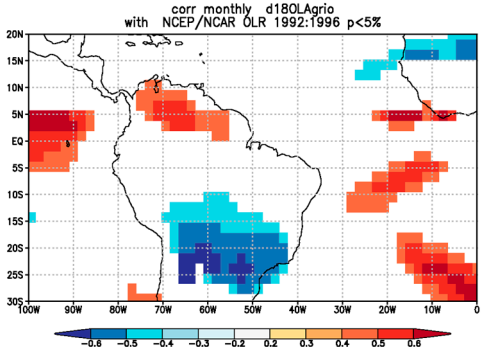

Nuevo Rocafuerte

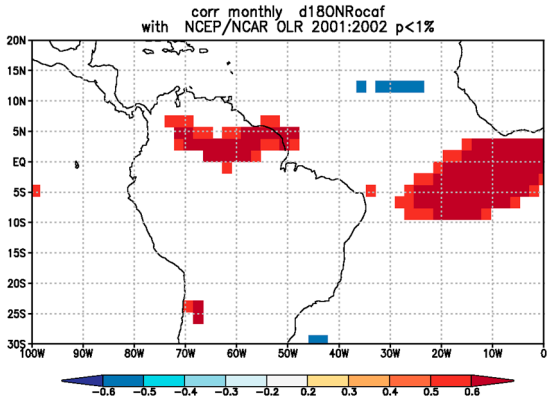

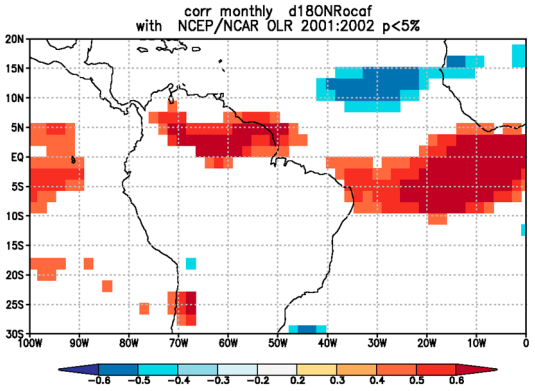

Izobamba

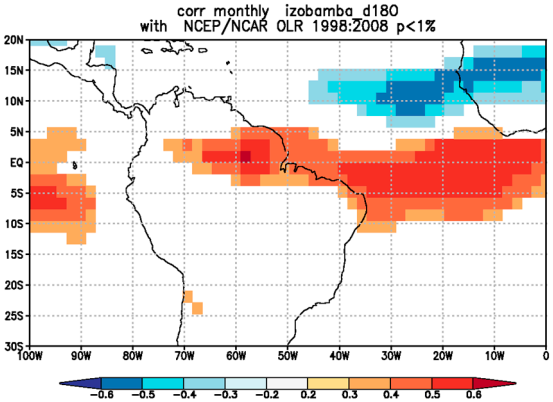

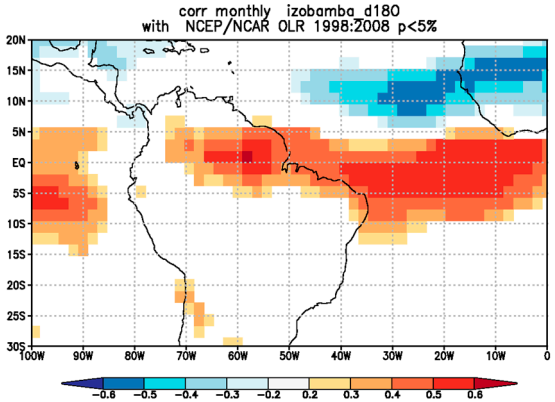

Quito

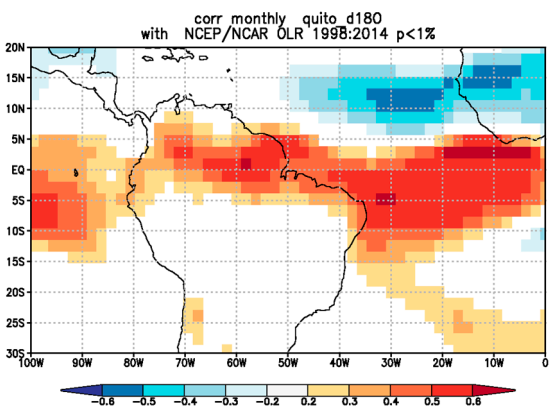

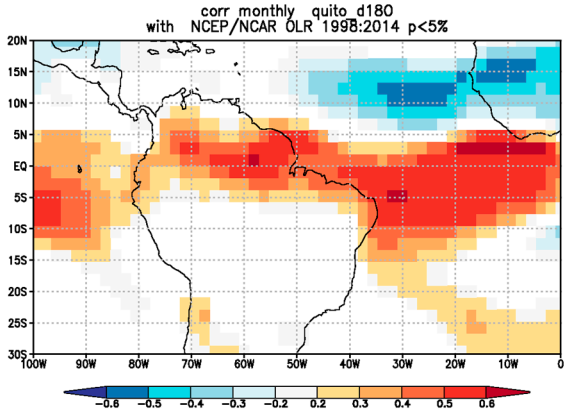

Papallacta

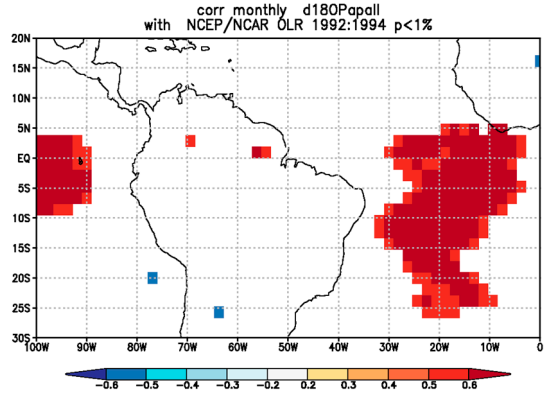

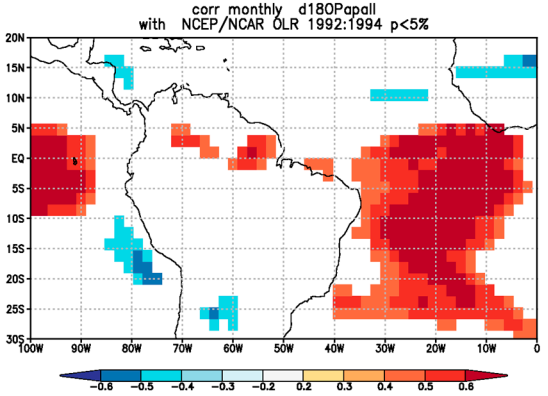

Mera

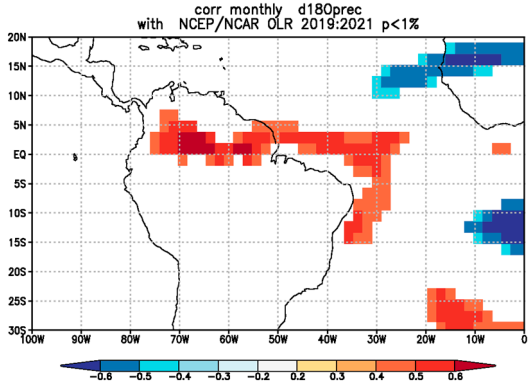

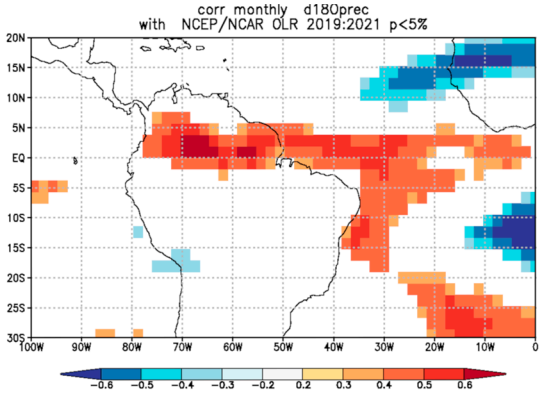

Amaluza

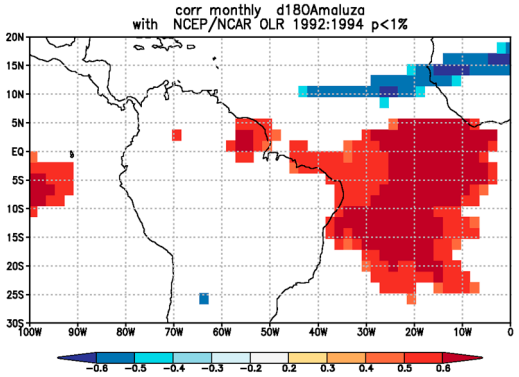

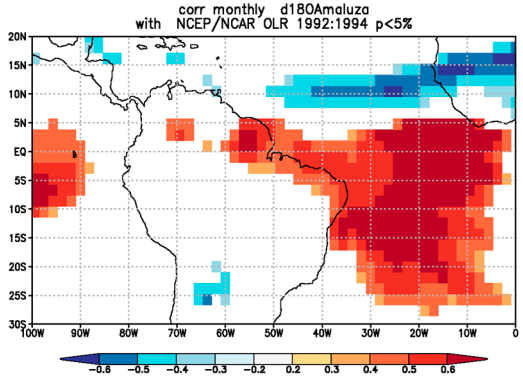

Mendez

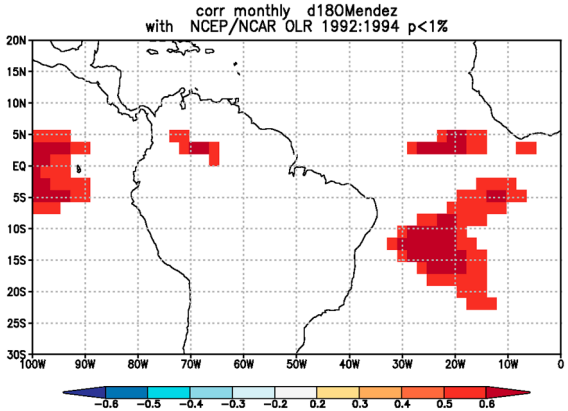

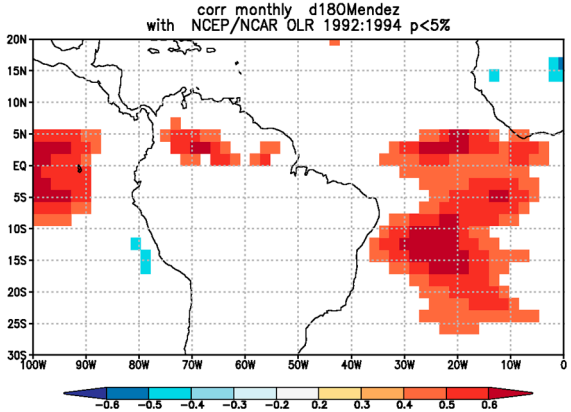

Cuenca

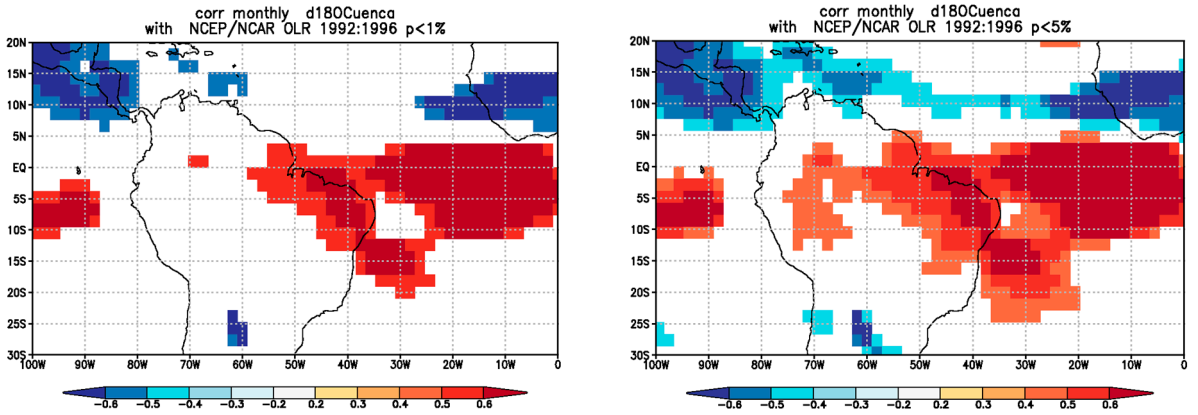

Bogotá

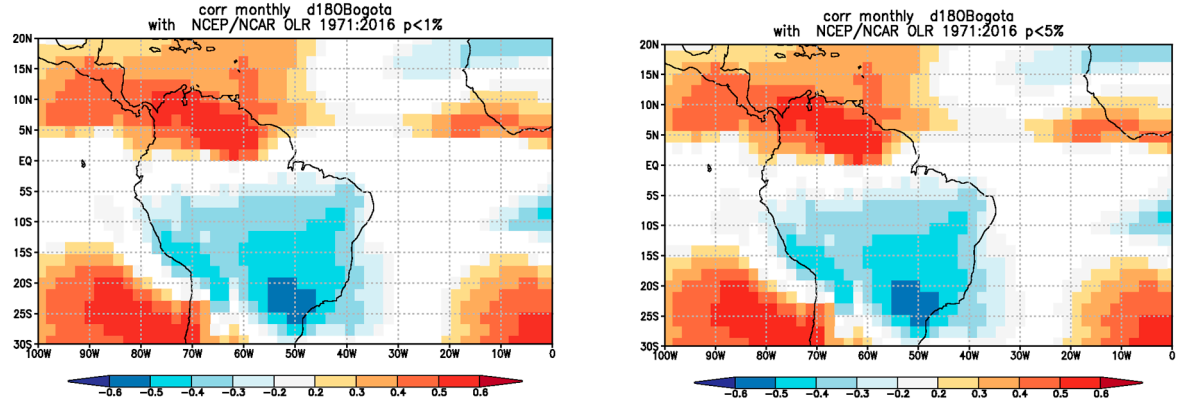

Figure S9. Spatial correlation between $\delta^{18}O$ in precipitation and Outgoing Longwave Radiation (OLR) at different stations along the inter-Andean valley and Amazon at $p<0.05$ and $p<0.01$. OLR data from the NOAA/OAR/ESRL PSL, Boulder, Colorado, USA, from their website at https://psl.noaa.gov/data. Analysis was calculated using the KNMI explorer [90].

References

36. Garcia, S.R.; Kayano, M.T. Some evidence on the relationship between the South American monsoon and the Atlantic ITCZ. *Theor. Appl. Climatol.* **2010**, *99*, 29–38. 10.1007/s00704-009-0107-z.

49. Warner, M.S.C. Introduction to PySPLIT: A Python Toolkit for NOAA ARL's HYSPLIT Model. *Comput. Sci. Eng.* **2018**, *20*, 47–62. 10.1109/MCSE.2017.3301549.

56. Liebmann, B.; Smith, C.A. Description of complete (interpolated) outgoing longwave radiation data set. *Bull. Amer. Meteor. Soc.* **1996**, *77*.

85. Uieda, L.; Tian, D.; Leong, W.J.; Toney, L.; Schlitzer, W.; Grund, M.; Newton, D.; Ziebarth, M.; Jones, M.; Wessel, P. PyGMT: A Python interface for the generic mapping tools. **2021**.

86. Wang, B.; Liu, J.; Kim, H.-J.; Webster, P.J.; Yim, S.-Y.; Xiang, B. Northern Hemisphere summer monsoon intensified by mega-El Nino/southern oscillation and Atlantic multidecadal oscillation. *Proc. Natl. Acad. Sci.* **2013**, *110*, 5347–5352. 10.1073/pnas.1219405110.

87. Douville, H.; Raghavan, K.; Renwick, J.; Allan, R.P.; Arias, P.A.; Barlow, M.; Cerezo-Mota, R.; Cherchi, A.; Gan, T.Y.; Gergis, J.; et al. *Water Cycle Changes. In Climate Change 2021: The Physical Science Basis. Contribution of Working Group I to the Sixth Assessment Report of the Intergovernmental Panel on Climate Change*; 2021;

88. Xie, P.; Arkin, P.A. Global Precipitation: A 17-Year Monthly Analysis Based on Gauge Observations, Satellite Estimates, and Numerical Model Outputs. *Bull. Am. Meteorol. Soc.* **1997**, *78*, 2539–2558. 10.1175/1520-0477(1997)078<2539:GPAYMA>2.0.CO;2.

89. Hersbach, H.; Bell, B.; Berrisford, P.; Biavati, G.; Horányi, A.; Muñoz Sabater, J.; Nicolas, J.; Peubey, C.; Radu, R.; Rozum, I.; et al. ERA5 monthly averaged data on single levels from 1979 to present. Copernicus Climate Change Service (C3S) Climate Data Store (CDS) Available online: https://cds.climate.copernicus.eu/ (accessed on Jul 10, 2021). 10.24381/cds.f17050d7.

90. Trouet, V.; Van Oldenborgh, G.J. KNMI Climate Explorer: A Web-Based Research Tool for High-Resolution Paleoclimatology. *Tree-Ring Res.* **2013**, *69*, 3–13. 10.3959/1536-1098-69.1.3.